

Direct observation of a magnetic-field-induced Wigner crystal

<https://doi.org/10.1038/s41586-024-07212-7>

Received: 2 December 2023

Accepted: 20 February 2024

Published online: 10 April 2024

 Check for updates

Yen-Chen Tsui^{1,6}, Minhao He^{1,6}, Yuwen Hu^{1,6}, Ethan Lake², Taige Wang^{2,3}, Kenji Watanabe⁴, Takashi Taniguchi⁵, Michael P. Zaletel^{2,3} & Ali Yazdani¹✉

Wigner predicted that when the Coulomb interactions between electrons become much stronger than their kinetic energy, electrons crystallize into a closely packed lattice¹. A variety of two-dimensional systems have shown evidence for Wigner crystals^{2–11} (WCs). However, a spontaneously formed classical or quantum WC has never been directly visualized. Neither the identification of the WC symmetry nor direct investigation of its melting has been accomplished. Here we use high-resolution scanning tunnelling microscopy measurements to directly image a magnetic-field-induced electron WC in Bernal-stacked bilayer graphene and examine its structural properties as a function of electron density, magnetic field and temperature. At high fields and the lowest temperature, we observe a triangular lattice electron WC in the lowest Landau level. The WC possesses the expected lattice constant and is robust between filling factor $v \approx 0.13$ and $v \approx 0.38$ except near fillings where it competes with fractional quantum Hall states. Increasing the density or temperature results in the melting of the WC into a liquid phase that is isotropic but has a modulated structure characterized by the Bragg wavevector of the WC. At low magnetic fields, the WC unexpectedly transitions into an anisotropic stripe phase, which has been commonly anticipated to form in higher Landau levels. Analysis of individual lattice sites shows signatures that may be related to the quantum zero-point motion of electrons in the WC lattice.

In low-density two-dimensional (2D) electronic systems, electrons are predicted to form a Wigner crystal (WC) when the ratio of the Coulomb energy to the kinetic energy becomes larger than about 40 (ref. 12). The application of a perpendicular magnetic field strongly suppresses the kinetic energy of an electron by forming Landau levels, thereby favouring WC formation at higher electron densities³, with its melting transition controlled by the filling factor of the Landau levels^{13,14}. A variety of 2D systems in both zero and high fields have shown evidence for electron crystallization using a wide range of experimental techniques. Most techniques^{2,4–11,15–26} provide indirect evidence for WC formation, making it difficult to distinguish between crystallization and localization by disorder, and are unable to provide information on the lattice structure and symmetry of the WC. The organization of electrons in a carbon nanotube in a pattern consistent with a small one-dimensional WC has been visualized²⁷. Although most 2D systems studied are inaccessible to imaging techniques, recent studies of transition metal dichalcogenide layers have succeeded in imaging generalized WC in zero magnetic field²⁸, the structures of which are dictated by a superlattice moiré potential that traps electrons. These crystalline electron phases are different from the WC phases expected to form spontaneously in the absence of any periodic potential and break continuous as opposed to discrete translational symmetry. Here we build on recent advances in scanning tunnelling microscopy (STM) studies

of ultra-clean graphene-based materials in high magnetic field^{29–33} to directly image WC lattice structure, visualize its melting and examine its competition with stripe ordering and fractional quantum Hall (FQH) states.

Evidence of the WC

STM measurements of ultra-clean bilayer graphene (BLG) devices have recently provided high-resolution spectroscopic measurements of a rich array of FQH states³³. These experiments have enabled probing FQH states in idealized conditions away from any defects, as well as fragile FQH states, such as the even-denominator candidate non-Abelian states, which have remarkably large energy gaps. The presence of sufficiently large defect-free areas in such devices (as shown in Fig. 1a) makes them ideal for visualizing WCs by spatially mapping the electronic properties of a partially filled Landau level. In this study, we focus on the filling range $0 < v < 1$, for which we have previously shown that electrons occupy the orbital state $N = 0$ in the top graphene layer³³. Figure 1b shows density-dependent scanning tunnelling spectroscopy (DD-STS) measurement in this filling range that shows a tunnelling Coulomb gap Δ_C near zero sample bias V_B (for tunnelling into a 2D electron gas at finite field³⁰), as well as features associated with the FQH states at $v = 1/3, 2/5, 3/7, 4/9$ and $5/11$. To probe the presence of a WC, we image

¹Joseph Henry Laboratories and Department of Physics, Princeton University, Princeton, NJ, USA. ²Department of Physics, University of California, Berkeley, Berkeley, CA, USA. ³Materials Sciences Division, Lawrence Berkeley National Laboratory, Berkeley, CA, USA. ⁴Research Center for Functional Materials, National Institute for Materials Science, Tsukuba, Japan. ⁵International Center for Materials Nanoarchitectonics, National Institute for Materials Science, Tsukuba, Japan. ⁶These authors contributed equally: Yen-Chen Tsui, Minhao He, Yuwen Hu. ✉e-mail: yazdani@princeton.edu

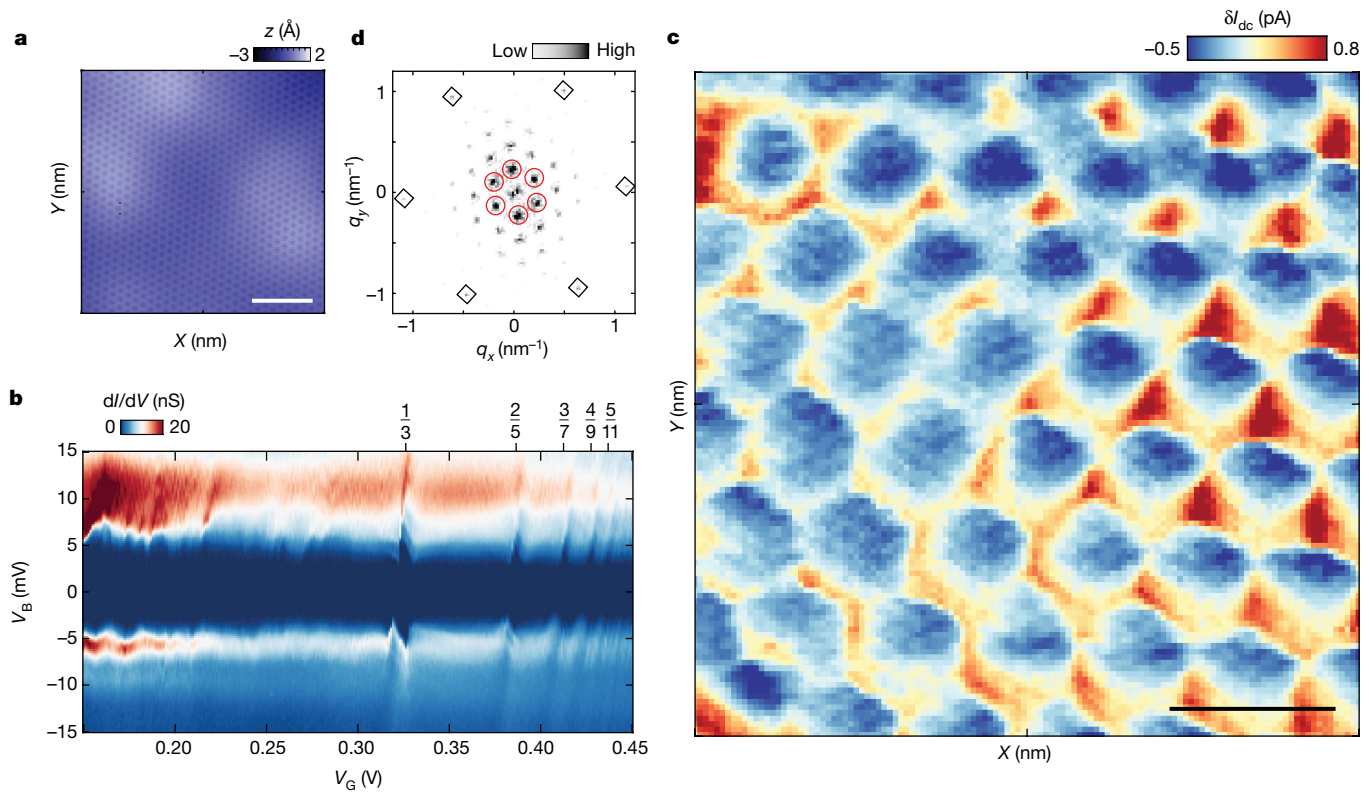


Fig. 1 | Emergent triangular lattice at partial filling of a $N=0$ Landau level in BLG. **a**, A topography image shows a clean surface without defects with setpoint $V_B = -0.2$ V, $I = 1$ nA. The periodic structure is the BLG/hBN moiré superlattice. **b**, DD-STS of a partially filled $N=0$ Landau level in BLG at magnetic field $B = 13.95$ T. The corresponding filling factors ν of the FQH states are marked on the top. **c**, Spatially resolved tunnelling current modulation δI_{dc}

within a 200 nm by 200 nm region (same area as in **a**). The measurement is taken with $V_B = 4.6$ mV at filling factor $\nu = 0.317$. **d**, FFT of the tunnelling current modulation δI_{dc} in **c**. The inner peaks in red circles are the first-order Bragg peaks of the emergent triangular lattice, whereas the outer peaks in black diamonds correspond to BLG/hBN moiré lattice with around 6.7 nm periodicity. Scale bars, 50 nm (**a**) and 50 nm (**c**).

the spatial modulation of the tunnelling current δI_{dc} at the threshold bias for electron tunnelling with V_B set at the edge of the Coulomb gap, while the STM feedback loop is disabled (Methods). These maps, an example of which is shown in Fig. 1c for $\nu = 0.317$, show a triangular lattice structure in the modulation of δI_{dc} , with a periodicity of near 30 nm that is consistent with that of an electron WC.

The fast Fourier transforms (FFTs) of δI_{dc} map for $\nu = 0.317$ (Fig. 1d) shows six first-order Bragg peaks (red circles) and many higher order peaks with well-defined C_6 symmetry, indicating a well-ordered WC in regions far from defects. The FFT also shows distinct peaks corresponding to a BLG/hBN incommensurate moiré superlattice (black diamonds) at length scales much smaller than that of the WC. Imaging the WC near defects, we see clear signatures that the WC is pinned (Supplementary Fig. 1). When performing STM imaging with electrons tunnelling from the tip into the sample ($V_B > 0$), we observe periodic suppression of tunnelling current and modulation of threshold bias voltage, suggesting that imaging contrast is related to the Coulomb suppression for electron tunnelling near the lattice sites of the WC, in which electrons are localized (Supplementary Fig. 2). Reversing the sample bias ($V_B < 0$) at the threshold for tunnelling, we observe an approximate reversal of imaging contrast and the enhancement of tunnelling current I_{dc} out of the sample correlated with the suppression of tunnelling at a positive bias (Extended Data Fig. 1). A priori, the potential produced by the STM tip, which contains a component in proportion to V_B , could locally distort or even drag the WC beneath the tip. However, as reversing V_B (at low bias) does not qualitatively affect our observations, this suggests that the impact of the tip-produced potential is minimal.

Examining the δI_{dc} map as a function of ν at the highest magnetic field and lowest temperature in our study (13.95 T, 210 mK electron temperature), we obtain precise measurements of the WC lattice structure that can be compared with theoretical predictions, as well as find evidence for melting of the WC and its competition with FQH states. Figure 2a–h shows a series of δI_{dc} maps measured in the same area while increasing ν (for the full data set, see Extended Data Figs. 2–4), which show the evolving spatial electronic structure of the partially filled Landau level. To analyse this evolution, we plot the corresponding structure factor $S(\mathbf{q})$ of the δI_{dc} maps in Fig. 2i–p, which are the FFTs of their autocorrelation maps (Methods). At low filling factors $\nu \approx 0.1$, the real space maps show distorted structures, with their $S(\mathbf{q})$ indicating the absence of an ordered WC presumably because of the importance of intrinsic disorder potential at low densities³⁴. By contrast, with increasing filling a well-ordered WC emerges showing a corresponding $S(\mathbf{q})$ with six sharp Bragg peaks, which show the simultaneous breaking of the translational and rotational symmetries, and the Bragg wavevectors disperse with increasing ν indicating the decreasing lattice constant (Fig. 2j–m). The continuously tuned peaks in $S(\mathbf{q})$ between $\nu \approx 0.15$ and $\nu \approx 0.31$ rotate between different densities (Fig. 2j–m), indicating that the orientationally ordered WC is not locked to any specific lattice potential (Supplementary Fig. 3). At the precise fillings corresponding to FQH states, such as $\nu = 1/3$ shown in Fig. 2f, $S(\mathbf{q})$ appears to be featureless, but more careful examination of the data near these FQH phases shows that the competition between WC and FQH states involves an intermediate liquid-like phase that has no orientational order (Supplementary Fig. 4). Increasing the filling, we find that WC remerges in between $\nu = 1/3$ and $2/5$, up to $\nu_{max} \approx 0.38$.

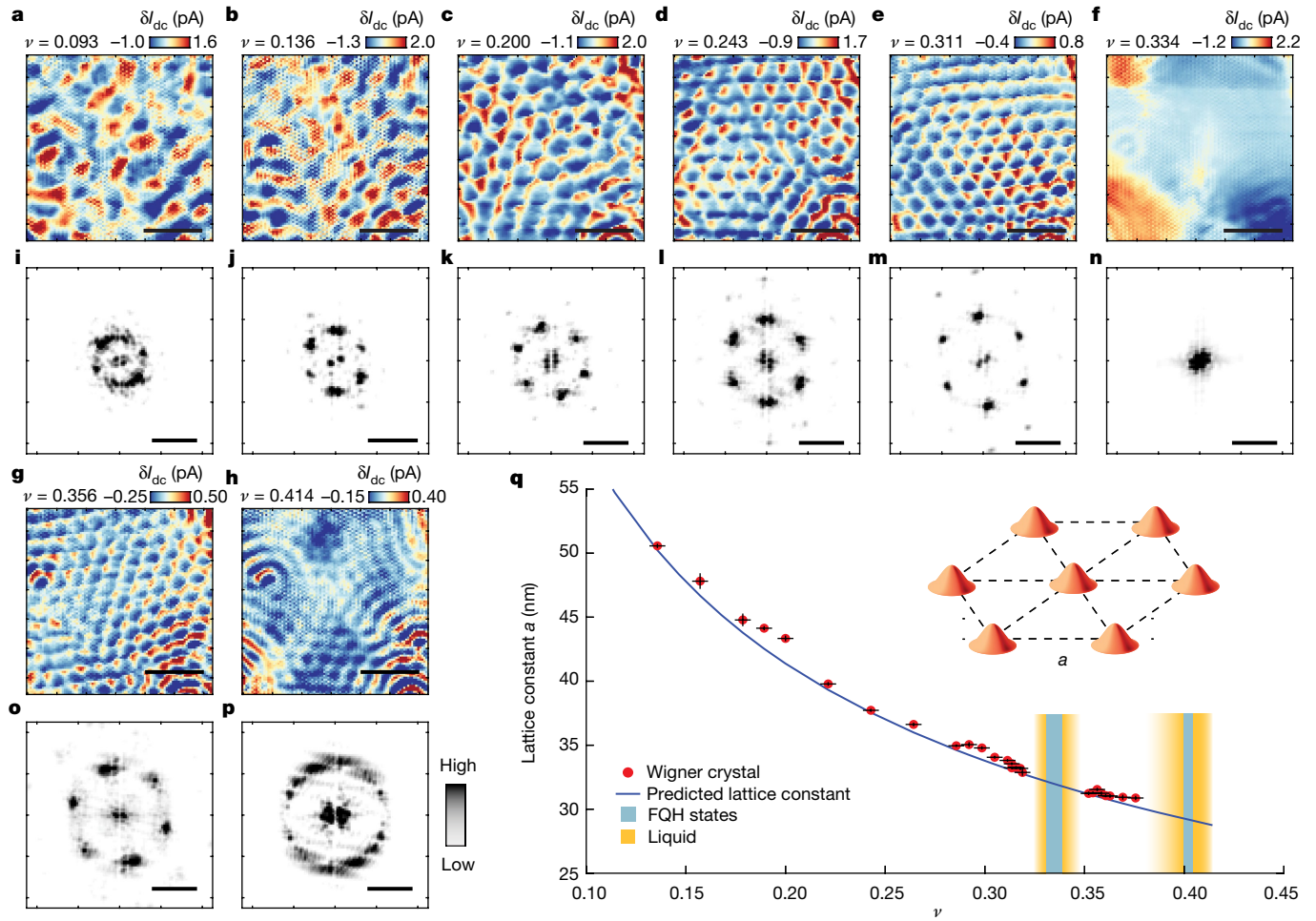


Fig. 2 | Identification of the WC. **a–h**, Spatially resolved tunnelling current modulation δI_{dc} of the same area measured at a series of different filling factor v , with $V_B = 5.2, 5.2, 4.6, 4.4, 4.4, 7.2, 8.0$ and 8.8 mV, respectively, at magnetic field $B = 13.95$ T. Scale bar, 100 nm. **i–p**, Structure factor $S(\mathbf{q})$ of the tunnelling current modulation δI_{dc} in **a–h** correspondingly. Scale bar, 0.2 nm^{-1} . **q**, The extracted lattice constant a of the emergent triangular lattice at different v (marked as solid red circles), measured in the same area at $B = 13.95$ T. The error bars in the

vertical direction represent the fitting error of determining a , and horizontal error bars denote the uncertainty of determination of the filling factor v (see Methods for more). The blue line is the expected periodicity of the WC. The blue-shaded regions mark the incompressible FQH states at $v = 1/3$ and $2/5$. The yellow-shaded regions mark the liquid phase. Inset, schematic of WC, consisting of electrons arranged in a triangular lattice with lattice constant a .

(Fig. 2g,o), but eventually at larger fillings it melts into a liquid phase (Fig. 2h) with $S(\mathbf{q})$ that shows a ring-like feature as shown in Fig. 2p (Extended Data Figs. 2–4).

To make a quantitative comparison with the predicted lattice constant of the WC, we extract the Bragg vectors $|\mathbf{q}|$ from the structure factor $S(\mathbf{q})$ maps (Methods) and calculate the corresponding triangular lattice constant $a = \frac{4\pi}{\sqrt{3}|\mathbf{q}|}$ as a function of v for data that show both translational and orientational orders. As shown in Fig. 2q, the experimental data follow the predicted lattice constant for the WC lattice $a = \sqrt{\frac{4\pi^2 B}{\sqrt{3}v}}$ (the blue curve) over a large range of v remarkably well and confirms that we are imaging a well-ordered WC. This agreement rules out other phases, such as the bubble phase, and also demonstrates that our measurement conditions are minimally perturbing the structure of the WC. We can also extend the Fourier analysis to the liquid phases by extracting the characteristic $|\mathbf{q}|$ from $S(\mathbf{q})$ maps and characterizing the modulations we observed in our δI_{dc} maps. Remarkably, the liquid phases near FQH phases, such as $1/3$ (Extended Data Fig. 5) and those at higher fillings (Extended Data Fig. 6), have a ring-like $S(\mathbf{q})$ that are characterized by a $|\mathbf{q}|$ very close to those for the WC at the same fillings.

The nature of quantum phase transition between WC and liquid phases such as FQH has been the subject of numerous theoretical studies.

The possibility of a first-order phase transition, its absence in the presence of disorder, the importance of the long-range Coulomb repulsion forbidding phase separation and prediction of the micro-emulsion intermediate phase, and crystallization of the fractionalized quasi-particles have all been considered^{35,36}. In the micro-emulsion scenario, which is relevant to singly-gated devices such as ours, domains of the competing phases interleave at a scale set by the gate distance (55 nm). Our observation of an intermediate liquid phase that appears to be uniform far from defects on length scales of 300 nm (Extended Data Figs. 2–4 and Supplementary Fig. 4 labelled as green circles) seems to be inconsistent with the possibility of modulated domains of WC and FQH. Examination on longer length scale in samples even cleaner than those studied here would be required to rule out this possibility. Our data does show some signature of inhomogeneous behaviour near the phase transition (Supplementary Fig. 4, labelled as yellow stars $v = 0.33–0.332$ and $0.335–0.342$, in which FQH and the intermediate liquid phase seem to coexist); however, they may be associated with defects rather than spontaneous phase separation or micro-emulsion.

The nature of our intermediate correlated liquid phases remains to be fully understood; however, they seem to be distinct from a Fermi liquid or composite Fermi liquid³⁷, which, in the presence of defects, is expected to have modulated electronic structure associated with

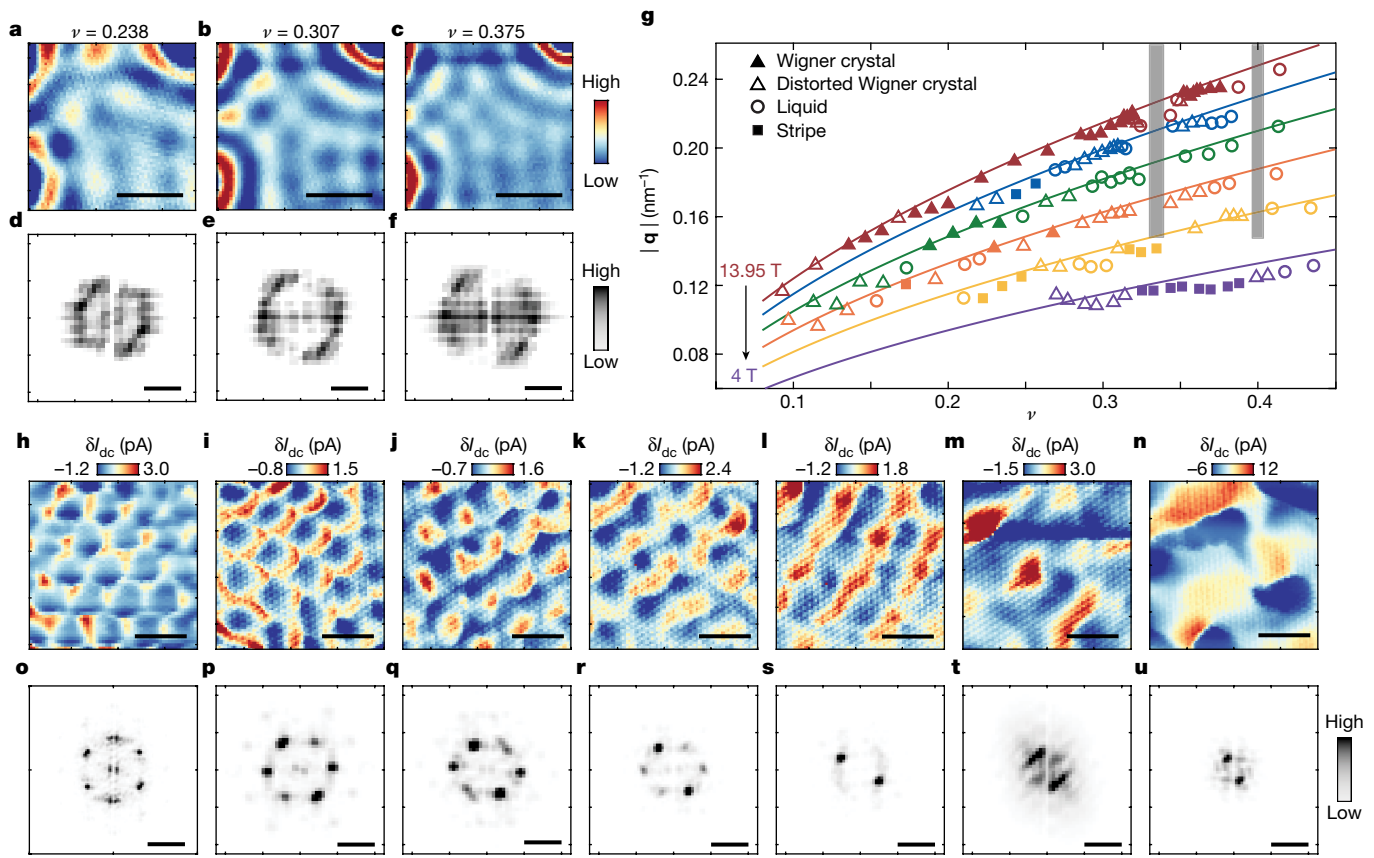


Fig. 3 | Temperature and magnetic field dependence of WC and observation of stripe phase. **a–c**, Tunnelling current modulation δI_{dc} measured at $B = 13$ T at $T \approx 3$ K. Scale bar, 50 nm. **d–f**, Structure factor $S(\mathbf{q})$ of δI_{dc} in **a–c**, showing ring-like liquid structure with changing periodicity. Scale bar, 0.2 nm $^{-1}$. **g**, Phase diagram of the electron WCs, distorted WCs, stripes and liquid states observed as a function of magnetic field B and filling factor ν . WC, distorted WC, liquid phase and stripe phase are represented by filled triangle, hollow triangle, hollow circle and filled square symbols, respectively. Each image is represented by $|q|$ of the Bragg peaks in the structure factor $S(\mathbf{q})$. Data are taken at $B = 13.95$ T (red), 12 T (blue), 10 T (green), 8 T (orange), 6 T (yellow) and 4 T (purple), in

which the solid lines represent the expected $|q|$ of the WC at corresponding B field. **h–n**, Spatially resolved tunnelling current modulation δI_{dc} measured at different magnetic fields $B = 13.95$ T (**h**), 12 T (**i**), 10 T (**j**), 8 T (**k**), 6 T (**l**), 4 T (**m**) and 2 T (**n**), with bias voltages $V_B = 5.2$ mV (**h**), 8.0 mV (**i**), 7.8 mV (**j**), 7.3 mV (**k**), 7.0 mV (**l**), 6.0 mV (**m**) and 3.0 mV (**n**). The measurements are performed at filling factor $\nu \approx 0.23$. Scale bar, 50 nm. **o–u**, Structure factor $S(\mathbf{q})$ of the tunnelling current modulation δI_{dc} in **h–n** correspondingly. The stripe phase forms at $B = 6$ T. At low field $B = 4$ T and 2 T, no periodic structure is observed. Scale bar, 0.2 nm $^{-1}$.

scattering on the (spin-polarized) Fermi surface at wavevector $2|\mathbf{k}_F| = 2\sqrt{4\pi n} = 2\sqrt{2\nu/l_B^2}$ where $|\mathbf{k}_F|$ is the amplitude of the Fermi wavevector at zero field and n is the electron density (Extended Data Fig. 6). One possibility is that a FQH state with dilute trapped quasi-particles may have liquid-like response for magneto-rotors at a $|\mathbf{q}|$, which have a dispersion minimum at $|\mathbf{q}|$ very close to that of the WC³⁸. An unknown intermediate phase is also possible; for example, at low magnetic fields Monte Carlo simulations of WC melting have shown the possibility of an intermediate ‘hybrid’ liquid-like phase³⁹. We add that the re-entrant behaviour of the WC between the 1/3 and 2/5 FQH states is similar to that previously reported from screening efficiency measurements on dilute 2D hole system in GaAs/AlGaAs heterostructure⁴⁰; however, the effective mass of this system is an order of magnitude larger than BLG⁴¹, which is thought to be responsible for its stability. A possible explanation of the stability of WC in BLG over a comparably wide filling range is the Landau level mixing between the orbital number $N = 0$ and 1 states, which might suppress nearby competing FQH states in favour of the WC.

Observation of the stripe phase

Having directly visualized the WC with the expected lattice structure and symmetry at a high magnetic field at our lowest temperature, we

turn our attention to its stability at lower fields and higher temperatures. Although we have not performed detailed temperature-dependent studies, the WC phase is observed to have melted at 3 K, with δI_{dc} showing liquid-like $S(\mathbf{q})$ (Fig. 3a–f and Supplementary Fig. 5). Lowering the magnetic field at the lowest temperatures (Fig. 3g and Supplementary Fig. 6), we find the WC becomes distorted, with $S(\mathbf{q})$ not showing all the expected six peaks of a well-ordered triangular lattice. At some fields and densities, the WC transforms into an unexpected stripe phase^{42–45} (Fig. 3l,s) with an orientation that is not correlated with any structural features of our sample, including small uniaxial heterostrain $\epsilon = 0.15\%$ induced by the moiré lattice⁴⁶, and which also rotates when we vary field or density (Supplementary Fig. 6). Figure 3g shows a detailed analysis of the field dependence of δI_{dc} maps for different fillings, annotating the different types of $S(\mathbf{q})$ feature characterizing the phases (WC, distorted WC, stripe and liquid phase) that are observed in each measurement, as well as their characteristic modulation wavevectors at each filling and magnetic field (see Methods and Supplementary Table 1 for phase characterization, full data set in Extended Data Figs. 2–4 and Supplementary Figs. 7–12). At low magnetic fields, the stability of the stripe phase is probably because of stronger Landau level mixing, which softens the Coulomb interaction as higher Landau level mixed in. Remarkably, both the stripe and liquid phases observed (at both low and high temperatures) are all characterized by a spatial modulation

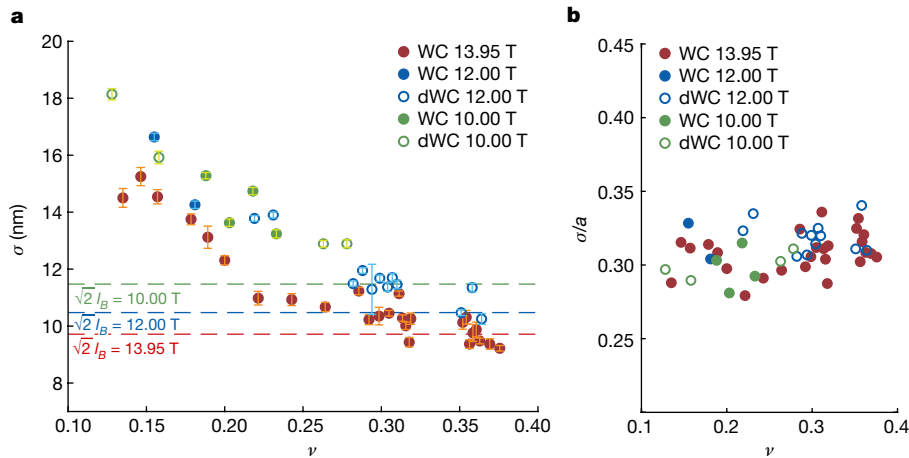


Fig. 4 | The quantum nature of the WC. **a**, Extracted variance σ of the WC sites versus filling factors ν at $B = 13.95$ T, 12.00 T and 10.00 T, represented by red, blue and green, respectively. The data points show a decreasing trend and saturates at high filling factors. The saturation value scales with magnetic length as around $\sqrt{2}l_B$. The solid circles and hollow circles stand for variance σ of the sites extracted from WC and distorted WC (dWC), respectively. The dashed

lines correspond to $\sqrt{2}l_B$ at each field. Error bars represent the fitting error using the Gaussian model (Methods). σ extracted for each field are from the data set measured in the same area. **b**, Ratio of the WC sites variance σ and lattice constant a , σ/a as a function of ν . The ratio remains at a high value of about 0.3 and is almost constant with respect to ν and to different fields.

corresponding to a $|\mathbf{q}|$ very close to that expected for a WC, at the same filling and magnetic fields. The strong correlations creating the WC still determine the structure of the correlated liquid and the stripe phases.

Quantum nature of the WC

Finally, we study the quantum and thermal fluctuations of the WC by investigating the spatial structure of individual WC sites. Of particular interest is the variance σ of the tunnelling current profile at each WC site, which we associate with the spatial extent of electron wavefunctions in the WC. An extraction of σ (Methods and Supplementary Fig. 13) yields the results presented in Fig. 4a, which show that as ν is increased, σ exhibits a pronounced decrease, followed by a saturation of approximately $\sqrt{2}l_B$ before melting. Remarkably, we observe the ratio σ/a to be rather large (around 0.3) and roughly independent of ν over a wide range of fillings and fields (Fig. 4b). The importance of quantum zero-point motion is typically captured using a quantity similar to our σ/a , the so-called de Boer parameter, which is the ratio of de Broglie wavelength to the lattice constant. The extreme example of a quantum crystal⁴⁷ is solid ^4He , with a de Boer parameter close to 0.4, which is larger but close to the value of $\sigma/a \approx 0.3$ for our WC. We also note that σ remains roughly unchanged even when the WC distorts and begins to melt at large ν , suggesting that the mechanism of melting is distinct from the usual Lindemann theory⁴⁸.

A minimal theoretical model addressing these observations is one in which the variance of electron positions is assumed to be caused by the phonon modes of the resulting WC. We have performed these calculations (Supplementary Information section 1.1) and find that the simplest model predicts a σ of about 30–50% lower than the observed value. The underestimation of σ suggests a smaller restoring force in the phonon model, which can be attributed to the softening of the Coulomb interaction because of screening and/or mixing of the $N=0$ and 1 Landau levels. A phonon model with RPA screening predicts σ 's that are closer to the experimental values at high ν (Supplementary Information section 1.1) but deviates at low fillings. This discrepancy and larger σ in general could also be because of the tip–sample interaction, which we expect to be stronger at lower ν , where the WC is softer and hence more easily to be distorted by the presence of the tip (Supplementary Information section 1.2). Disentangling the role of softened Coulomb interaction from tip perturbations requires further systematic measurements as a function of temperature and tunnelling bias V_B .

Discussion

Looking ahead, our imaging technique can potentially be used to examine a wide range of spatially modulated electronic phases, including hole WC, WC at zero magnetic field, bilayer WC, skyrme crystal, bubble phases and possibly WC of quasi-particles found near FQH states. Detailed structural studies could also be used to examine the mechanism of melting such as topological-defect-mediated melting mechanism^{49,50}. Measurements in the presence of a net electrical current flowing through the device could also be used to explore the depinning of a WC from the disorder potential.

Online content

Any methods, additional references, Nature Portfolio reporting summaries, source data, extended data, supplementary information, acknowledgements, peer review information; details of author contributions and competing interests; and statements of data and code availability are available at <https://doi.org/10.1038/s41586-024-07212-7>.

1. Wigner, E. On the interaction of electrons in metals. *Phys. Rev.* **46**, 1002–1011 (1934).
2. Grimes, C. C. & Adams, G. Evidence for a liquid-to-crystal phase transition in a classical, two-dimensional sheet of electrons. *Phys. Rev. Lett.* **42**, 795–798 (1979).
3. Lozovik, Y. E. & Budson, V. I. Crystallization of a two-dimensional electron gas in a magnetic field. *J. Exp. Theor. Phys. Lett.* **22**, 11–12 (1975).
4. Andrei, E. Y. et al. Observation of a magnetically induced Wigner solid. *Phys. Rev. Lett.* **60**, 2765–2768 (1988).
5. Santos, M. B. et al. Observation of a reentrant insulating phase near the 1/3 fractional quantum Hall liquid in a two-dimensional hole system. *Phys. Rev. Lett.* **68**, 1188–1191 (1991).
6. Yoon, J., Li, C. C., Shahar, D., Tsui, D. C. & Shayegan, M. Wigner crystallization and metal-insulator transition of two-dimensional holes in GaAs at $B=0$. *Phys. Rev. Lett.* **82**, 1744–1747 (1999).
7. Hossain, M. S. et al. Observation of spontaneous ferromagnetism in a two-dimensional electron system. *Proc. Natl Acad. Sci. USA* **117**, 32244–32250 (2020).
8. Smołenski, T. et al. Signatures of Wigner crystal of electrons in a monolayer semiconductor. *Nature* **595**, 53–57 (2021).
9. Zhou, Y. et al. Bilayer Wigner crystals in a transition metal dichalcogenide heterostructure. *Nature* **595**, 48–52 (2021).
10. Yang, F. et al. Experimental determination of the energy per particle in partially filled Landau levels. *Phys. Rev. Lett.* **126**, 156802 (2021).
11. Falson, J. et al. Competing correlated states around the zero-field Wigner crystallization transition of electrons in two dimensions. *Nat. Mater.* **21**, 311–316 (2022).
12. Tanatar, B. & Ceperley, D. M. Ground state of the two-dimensional electron gas. *Phys. Rev. B* **39**, 5005–5016 (1989).
13. Levesque, D., Weis, J. J. & MacDonald, A. H. Crystallization of the incompressible quantum-fluid state of a two-dimensional electron gas in a strong magnetic field. *Phys. Rev. B* **30**, 1056–1058 (1984).

14. Lam, P. K. & Girvin, S. M. Liquid-solid transition and the fractional quantum-Hall effect. *Phys. Rev. B* **30**, 473–475 (1984).
15. Tiemann, L., Rhone, T. D., Shibata, N. & Muraki, K. NMR profiling of quantum electron solids in high magnetic fields. *Nat. Phys.* **10**, 648–652 (2014).
16. Willett, R. L. et al. Termination of the series of fractional quantum hall states at small filling factors. *Phys. Rev. B* **38**, 7881–7884 (1988).
17. Goldman, V. J., Santos, M., Shayegan, M. & Cunningham, J. E. Evidence for two-dimensional quantum Wigner crystal. *Phys. Rev. Lett.* **65**, 2189–2192 (1990).
18. Buhmann, H. et al. Novel magneto-optical behavior in the Wigner-solid regime. *Phys. Rev. Lett.* **66**, 926–929 (1990).
19. Jiang, H. W. et al. Quantum liquid versus electron solid around $v=1/5$ Landau-level filling. *Phys. Rev. Lett.* **65**, 633–636 (1990).
20. Li, Y. P., Sajoto, T., Engel, L. W., Tsui, D. C. & Shayegan, M. Low-frequency noise in the reentrant insulating phase around the 1/5 fractional quantum Hall liquid. *Phys. Rev. Lett.* **67**, 1630–1633 (1991).
21. Paalanen, M. A. et al. rf conductivity of a two-dimensional electron system at small Landau-level filling factors. *Phys. Rev. B* **45**, 11342–11345 (1992).
22. Ye, P. D. et al. Correlation lengths of the Wigner-crystal order in a two-dimensional electron system at high magnetic fields. *Phys. Rev. Lett.* **89**, 176802 (2002).
23. Chen, Y. P. et al. Melting of a 2D quantum electron solid in high magnetic field. *Nat. Phys.* **2**, 452–455 (2006).
24. Zhang, D., Huang, X., Dietsche, W., Klitzing, K. v. & Smet, J. H. Signatures for Wigner crystal formation in the chemical potential of a two-dimensional electron system. *Phys. Rev. Lett.* **113**, 076804 (2014).
25. Deng, H. et al. Commensurability oscillations of composite fermions induced by the periodic potential of a Wigner crystal. *Phys. Rev. Lett.* **117**, 096601 (2016).
26. Jang, J., Hunt, B. M., Pfeiffer, L. N., West, K. W. & Ashoori, R. C. Sharp tunnelling resonance from the vibrations of an electronic Wigner crystal. *Nat. Phys.* **13**, 340–344 (2017).
27. Shapir, I. et al. Imaging the electronic Wigner crystal in one dimension. *Science* **364**, 870–875 (2019).
28. Li, H. et al. Imaging two-dimensional generalized Wigner crystals. *Nature* **597**, 650–654 (2021).
29. Li, S.-Y., Zhang, Y., Yin, L.-J. & He, L. Scanning tunneling microscope study of quantum Hall isospin ferromagnetic states in the zero Landau level in a graphene monolayer. *Phys. Rev. B* **100**, 085437 (2019).
30. Liu, X. et al. Visualizing broken symmetry and topological defects in a quantum Hall ferromagnet. *Science* **375**, 321–326 (2021).
31. Coissard, A. et al. Imaging tunable quantum Hall broken-symmetry orders in graphene. *Nature* **605**, 51–56 (2022).
32. Farahi, G. et al. Broken symmetries and excitation spectra of interacting electrons in partially filled Landau levels. *Nat. Phys.* **19**, 1482–1488 (2023).
33. Hu, Y. et al. High-resolution tunneling spectroscopy of fractional quantum Hall states. Preprint at arxiv.org/abs/2308.05789 (2023).
34. Aoki, H. Effect of coexistence of random potential and electron-electron interaction in two-dimensional systems: Wigner glass. *J. Phys. C Solid State Phys.* **12**, 633 (2001).
35. Spivak, B. & Kivelson, S. A. Phases intermediate between a two-dimensional electron liquid and Wigner crystal. *Phys. Rev. B* **70**, 155114 (2004).
36. Zhu, X. & Louie, S. G. Wigner crystallization in the fractional quantum Hall regime: a variational quantum Monte Carlo study. *Phys. Rev. Lett.* **70**, 335–338 (1993).
37. Halperin, B. I., Lee, P. A. & Read, N. Theory of the half-filled Landau level. *Phys. Rev. B* **47**, 7312–7343 (1993).
38. Girvin, S. M., MacDonald, A. H. & Platzman, P. M. Magneto-roton theory of collective excitations in the fractional quantum Hall effect. *Phys. Rev. B* **33**, 2481–2494 (1986).
39. Falakshahi, H. & Waintal, X. Hybrid phase at the quantum melting of the Wigner crystal. *Phys. Rev. Lett.* **94**, 046801 (2005).
40. Ma, M. K. et al. Thermal and quantum melting phase diagrams for a magnetic-field-induced Wigner solid. *Phys. Rev. Lett.* **125**, 036601 (2020).
41. Zou, K., Hong, X. & Zhu, J. Effective mass of electrons and holes in bilayer graphene: electron-hole asymmetry and electron-electron interaction. *Phys. Rev. B* **84**, 085408 (2011).
42. Koulakov, A. A., Fogler, M. M. & Shklovskii, B. I. Charge density wave in two-dimensional electron liquid in weak magnetic field. *Phys. Rev. Lett.* **76**, 499–502 (1995).
43. Fradkin, E. & Kivelson, S. A. Liquid-crystal phases of quantum Hall systems. *Phys. Rev. B* **59**, 8065–8072 (1999).
44. Lilly, M. P., Cooper, K. B., Eisenstein, J. P., Pfeiffer, L. N. & West, K. W. Evidence for an anisotropic state of two-dimensional electrons in high Landau levels. *Phys. Rev. Lett.* **82**, 394–397 (1999).
45. Du, R. R. et al. Strongly anisotropic transport in higher two-dimensional Landau levels. *Solid State Commun.* **109**, 389–394 (1999).
46. Kerenky, A. et al. Maximized electron interactions at the magic angle in twisted bilayer graphene. *Nature* **572**, 95–100 (2019).
47. Cazorla, C. & Boronat, J. Simulation and understanding of atomic and molecular quantum crystals. *Rev. Mod. Phys.* **89**, 035003 (2017).
48. Lindemann, F. About the calculation of molecular own frequencies. *Z. Phys.* **11**, 609–612 (1910).
49. Kosterlitz, J. M. & Thouless, D. J. Ordering, metastability and phase transitions in two-dimensional systems. *J. Phys. C Solid State Phys.* **6**, 1181 (1973).
50. Halperin, B. I. & Nelson, D. R. Theory of two-dimensional melting. *Phys. Rev. Lett.* **41**, 121–124 (1978).

Publisher's note Springer Nature remains neutral with regard to jurisdictional claims in published maps and institutional affiliations.

Springer Nature or its licensor (e.g. a society or other partner) holds exclusive rights to this article under a publishing agreement with the author(s) or other rightsholder(s); author self-archiving of the accepted manuscript version of this article is solely governed by the terms of such publishing agreement and applicable law.

© The Author(s), under exclusive licence to Springer Nature Limited 2024

Methods

Sample preparation

The BLG devices are fabricated with a modified dry transfer method. The heterostructure consists of exfoliated BLG/hBN/few-layer graphite layers from top to bottom. The heterostructure is picked up by a poly-vinyl alcohol (PVA) handle, supported by a transparent tape on poly-dimethylsiloxane (PDMS) and then transferred onto a pre-patterned SiO₂ (285 nm)/Si substrate with Au/Ti contacts (50 nm/3 nm). We focus on a device with the hBN dielectric layer of 55 nm in this study. The PVA film is first dissolved in HPLC water. Then the sample surface is extensively cleaned in a series of solvents, including HPLC water, acetone, isopropyl alcohol and *n*-methyl-2-pyrrolidone (NMP). The device is then transferred into the ultrahigh vacuum chamber to anneal at 475 °C overnight before transferring into STM.

STM measurement

STM experiment is performed in a custom-built dilution refrigerator STM with a mixing chamber temperature of about 20 mK and an effective electron temperature $T_{\text{eff}} \approx 210$ mK calibrated on a single crystal Al(100) unless specified. Data in this paper are obtained with a perpendicular magnetic field ranging from 2 T to 13.95 T. The measurements are performed using tungsten tips carefully prepared on Cu(111) surface to minimize the work function mismatch between the tip and the sample³².

The measurements are performed with the tip grounded and a bias voltage V_B applied to the BLG. A total of $V_B + V_G$ is applied to the graphite back gate to maintain a relative V_G difference between the sample and the back gate. The differential conductance d/dV is taken by the lock-in method with a.c. modulation at a frequency of 712.9 Hz in typical STS measurements.

The large area tunnelling current map (δI_{dc} map) is taken with the following procedure.

For each line of the map, the first forward and backward scan is performed with a setpoint $V_B = -0.2$ V, $I = 1$ nA at constant current mode to record the topography corrugation z (the typical scan speed is approximately 3 s per line). For the second forward and backward scan, the tip returns to its starting position and then follows the recorded forward and backward height z (with feedback disabled) with a small bias voltage V_B close to the Fermi energy and records the d.c. current channel I_{dc} at the same time. Finally, the tip returns to its starting position of each line, moves upwards to the next pixel and then repeats the above line scan until the map is done. To capture the underlying electronic structure clearly, we present the spatial modulation of the d.c. tunnelling current δI_{dc} by subtracting its line average: $\delta I_{\text{dc}} = |I_{\text{dc}}| - \langle |I_{\text{dc}}| \rangle_{\text{line}}$. Note that for $V_B > 0$, $\delta I_{\text{dc}} = I_{\text{dc}} - \langle I_{\text{dc}} \rangle_{\text{line}}$ because the current is always positive; whereas for $V_B < 0$, $\delta I_{\text{dc}} = -(I_{\text{dc}} - \langle I_{\text{dc}} \rangle_{\text{line}})$ because the current is negative. Therefore, large δI_{dc} means the enhancement of the current signal, whereas small δI_{dc} means the suppression of the current. Note that for $V_B > 0$, positive d.c. current I_{dc} is always obtained, whereas its spatial modulation δI_{dc} could be a negative value; for $V_B < 0$, negative d.c. current I_{dc} is always obtained, whereas its spatial modulation δI_{dc} could be a positive value as indicated in the colour bar.

The tunnelling current map (δI_{dc} map) gives the same spatial information as the differential conductance d/dV maps when measured with a small bias voltage V_B close to the edge of the Coulomb gap (Supplementary Fig. 17). In this study, we present the δI_{dc} maps instead of d/dV maps for their higher signal-to-noise ratio and shorter integration time required.

Structure factor $S(\mathbf{q})$ extraction

The structure factor of the δI_{dc} map is defined as $S(\mathbf{q}) = \langle \delta I_{\text{dc}}(\mathbf{q}) \times \delta I_{\text{dc}}(-\mathbf{q}) \rangle$, where $\delta I_{\text{dc}}(\mathbf{q}) = \int \delta I_{\text{dc}}(\mathbf{r}) e^{i\mathbf{q} \cdot \mathbf{r}} d\mathbf{r}$. Mathematically, the Fourier transform of an autocorrelation function (ACF) of the δI_{dc} map, which is the power spectral density, is equivalent to the modulus-squared

fast Fourier transform map of the δI_{dc} map ($|\delta I_{\text{dc}}(\mathbf{q})|^2 = S(\mathbf{q})$). In practice, an ACF map of the δI_{dc} is first obtained with zero padding, and the structure factor $S(\mathbf{q})$ map is then generated by taking a fast Fourier transform of the ACF map.

Determination of the lattice constant a

The lattice constant a is obtained from the reciprocal relation $\mathbf{a}_i \cdot \mathbf{q}_j = 2\pi\delta_{ij}$, where we have $a = \frac{2\pi}{|\mathbf{q}|} \times \frac{2}{\sqrt{3}}$ for the triangular lattice of a WC. The $|\mathbf{q}|$ is obtained from the structure factor $S(\mathbf{q})$ map: The $S(\mathbf{q})$ map is first converted into polar coordinates (ρ, θ) and then averaged over θ . $|\mathbf{q}|$ is then extracted by performing a Gaussian fit to the location of the Bragg peak. This determines the fitting error bar of the $|\mathbf{q}|$. The 95% confidence interval of $|\mathbf{q}|$ is then converted to the 95% confidence interval of corresponding lattice constant a , from where we determine its error bar.

Correspondingly, the filling factor v is converted from gate voltage V_G by assuming a geometric capacitance within a Landau level sector; therefore, its uncertainty comes from ignoring the quantum capacitance inside the FQH gaps. The uncertainty of v is estimated by the FQH states (the ones with large denominators) that we can confidently assign, which is upper bounded by a value of the fractions $8/17 - 7/15 \approx 0.004$ (ref. 33).

Determination of the electronic ground state

The electronic ground states are assigned mainly according to the structure factor $S(\mathbf{q})$ map of measurements at each filling factor and magnetic field, assisted by the corresponding δI_{dc} map and its ACF. Images with six distinguishable Bragg peaks in $S(\mathbf{q})$ map can be identified with quasi-long-range translational order and quasi-long-range orientational order, and thus are identified as WCs. Images with distorted, azimuthally broadened or interconnected six Bragg peaks in $S(\mathbf{q})$ are assigned as distorted WCs because of the lack of quasi-long-range translational order or orientational order. Images with ring-like features in $S(\mathbf{q})$ and an isotropic electronic ground state, with the corresponding δI_{dc} map showing interference patterns of concentric ring-like structures centred at disorder locations are assigned as liquid states. Images with two main Bragg peaks in $S(\mathbf{q})$ and strongly anisotropic features in the corresponding δI_{dc} map are assigned as stripe phases.

Extraction of the variance σ of an electron site

The variance σ of electron sites is extracted from areas far from impurities, in images identified as WC or distorted WC (see Supplementary Fig. 13, for example). The locations of the electron sites are first determined as (x_i, y_i) , $i = 1, 2, \dots, N$, with N being the number of electron sites within the fitting range. The simulated WC lattice consists of electrons on each site with a wavefunction of a Gaussian form, as expected in the Landau level with orbital number $N = 0$. The Gaussians are placed on each site with the same variance σ and the same amplitude A as fitting parameters, resulting in an electron distribution function:

$$\sum_{i=1}^N Ae^{-\frac{(x-x_i)^2+(y-y_i)^2}{2\sigma^2}}$$

This distribution function is then used to fit the normalized tunnelling current modulation δI_{dc} to find the averaged variance σ of electron sites. We interpret σ as the size of an electron site in the WC phase.

The variance σ fitted above reflects information within a local fitting range, which can vary from region to region depending on the microscopic details such as disorder potential. Measurements at different regions on the sample are performed to extract σ following the same procedure. The variance of the σ , from region to region, is estimated to be about 0.50 nm, which is interpreted as a statistical error of σ (distinct from the fitting error as shown in Fig. 4a).

Article

Data availability

Other data that support the findings of this study are available from the corresponding author upon request. Source data are provided with this paper for the main figures and Extended Data figures.

Acknowledgements We acknowledge fruitful discussions with D. Huse, S. Kivelson and M. Heiblum. This work was primarily supported by DOE-BES grant DE-FG02-07ER46419 and the EPIQS initiative grants GBMF9469 of the Gordon and Betty Moore Foundation to A.Y. Other support for the experimental infrastructure was provided by NSF-MRSEC through the Princeton Center for Complex Materials NSF-DMR-2011750, DMR-2312311, ARO MURI (W911NF-21-2-0147) and ONR N00012-21-1-2592. A.Y. acknowledges the hospitality of the Aspen Center for Physics, which is supported by National Science Foundation grant PHY-1607611, where part of this work was carried out. M.P.Z. and T.W. were supported by the US Department of Energy, Office of Science, Office of Basic Energy Sciences, Materials Sciences and

Engineering Division, under contract no. DE-AC02-05CH11231, in the van der Waals Heterostructures Program (KCWF16).

Author contributions Y.-C.T., M.H., Y.H. and A.Y. devised the experiments; Y.-C.T., M.H. and Y.H. created the structures of the devices and carried out the STM measurements and data analysis. E.L., T.W. and M.P.Z. carried out the theoretical calculations. K.W. and T.T. provided the h-BN substrates. All authors contributed to the writing of the paper.

Competing interests The authors declare no competing interests.

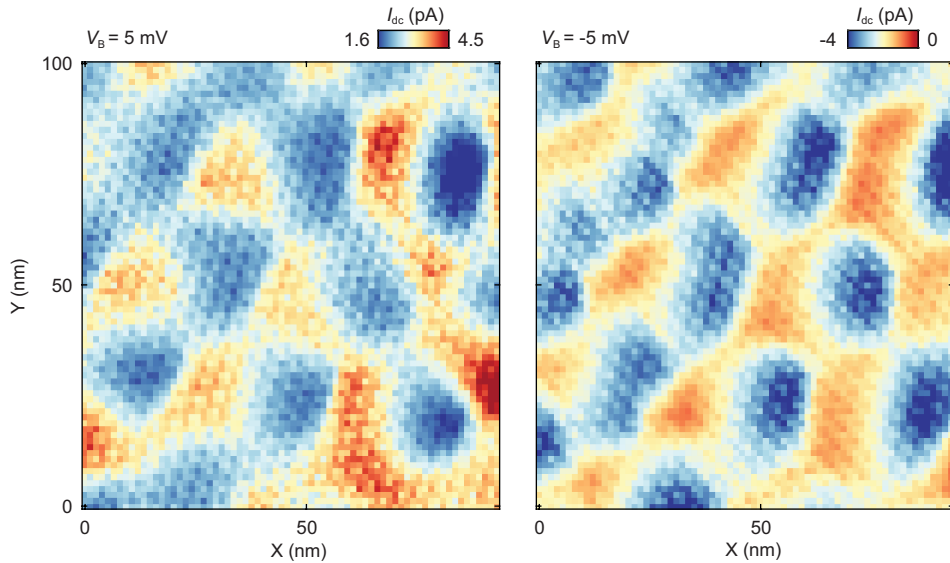
Additional information

Supplementary information The online version contains supplementary material available at <https://doi.org/10.1038/s41586-024-07212-7>.

Correspondence and requests for materials should be addressed to Ali Yazdani.

Peer review information *Nature* thanks Benjamin Sacepe and the other, anonymous, reviewer(s) for their contribution to the peer review of this work.

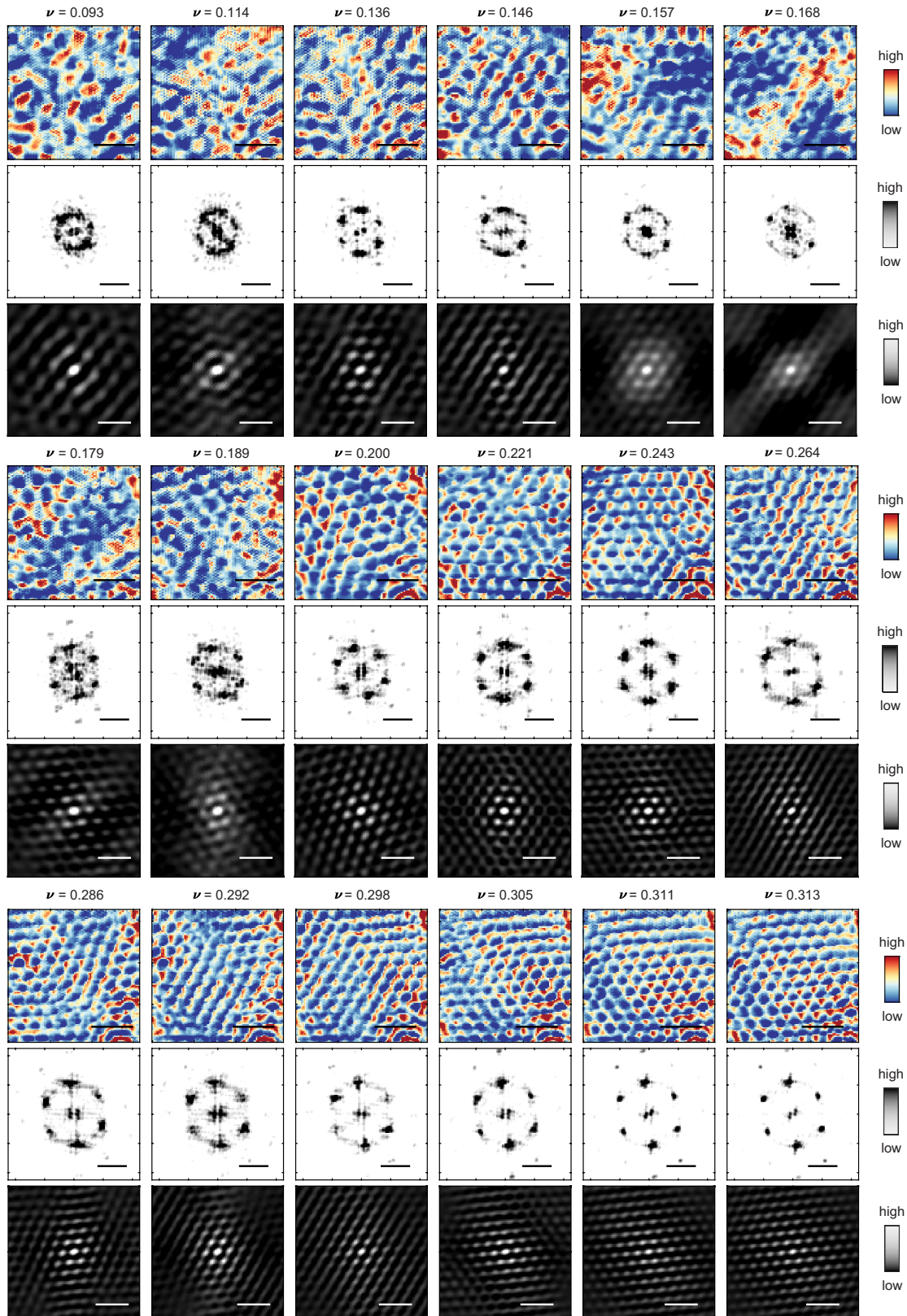
Reprints and permissions information is available at <http://www.nature.com/reprints>.



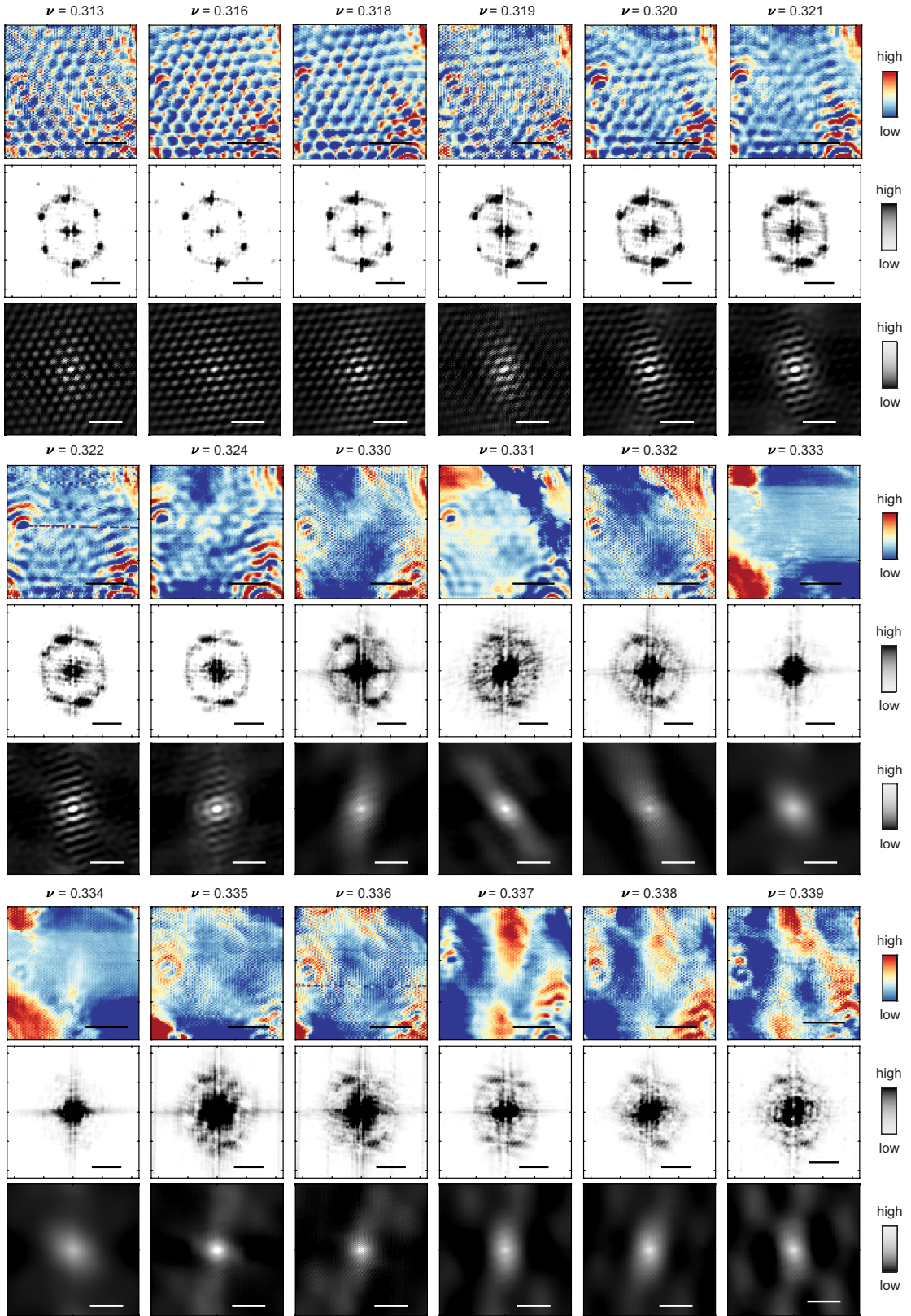
Extended Data Fig. 1 | Effects of the bias voltage V_B on the Wigner crystal images. The two I_{dc} images show the WC imaged at the same area, same v with different bias voltages. Left: $V_B = 5$ mV; right: $V_B = -5$ mV. Notice that the $I_{dc} > 0$ for $V_B > 0$, and $I_{dc} < 0$ for $V_B < 0$. With the bias voltage V_B applied on the sample and the tip grounded, the electron is tunneled from tip (sample) to the sample (tip) for positive (negative) bias voltage V_B . The observed suppression (enhancement) of current indicates the presence of a localized electron. When $V_B > 0$, a larger energy penalty is required for tunneling into the site, therefore a suppression of the current for a fixed bias voltage image; whereas for $V_B < 0$, since there's an extra charge to contribute from the site, an enhancement of the

current for a fixed bias voltage image is expected. However, a slight shift of the positions of the sites is detected in these images with reversed bias, along with slight shape changes. These observations could potentially be explained by the tip perturbation. For example, it could be tip gating effects which can slightly change the local filling factor v , resulting in the slight shift. Other than potential local gating from tip, the spatial shift of the localized electron might also be explained as results of a small horizontal electric field E (in the graphene sample) from voltage V_t (sum of work function mismatch and bias voltage V_B) which is different for measurements taken at positive/negative coulomb gap edges. Other possibility, such as the piezo drifting effect has been excluded.

Article

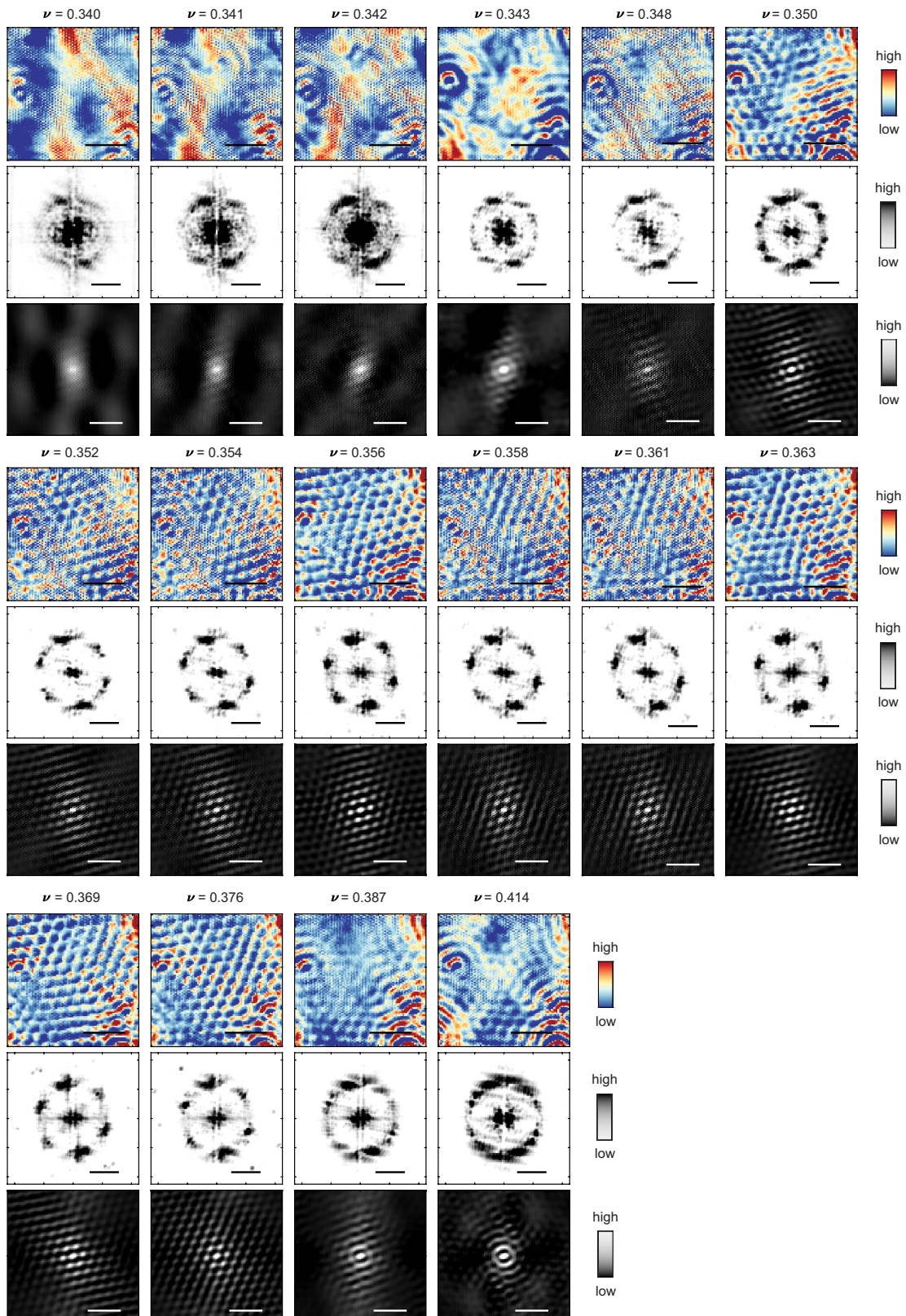


Extended Data Fig. 2 | Full data set (I) of electronic ground state imaging at $B=13.95\text{ T}$. The data are presented in the sequence in rows of $\delta I_{dc} S(q)$, and autocorrelation of δI_{dc} . The filling factor ν of each set is noted on the top. The scale bars for $\delta I_{dc}, S(q)$, autocorrelation of δI_{dc} are 100 nm, 0.2 nm⁻¹, 100 nm, respectively.

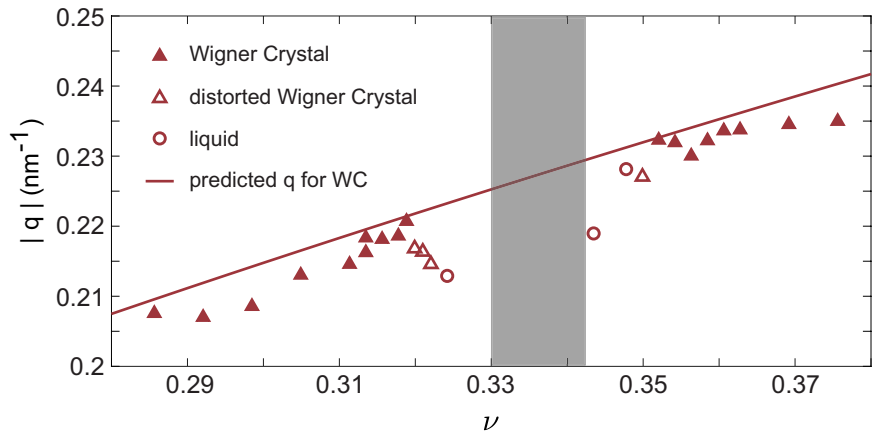


Extended Data Fig. 3 | Full data set (II) of electronic ground state imaging at $B=13.95$ T. The data are presented in the sequence in rows of δI_{dc} , $S(q)$, and autocorrelation of δI_{dc} . The filling factor ν of each set is noted on the top. The scale bars for δI_{dc} , $S(q)$, autocorrelation of δI_{dc} are 100 nm, 0.2 nm⁻¹, 100 nm, respectively.

Article

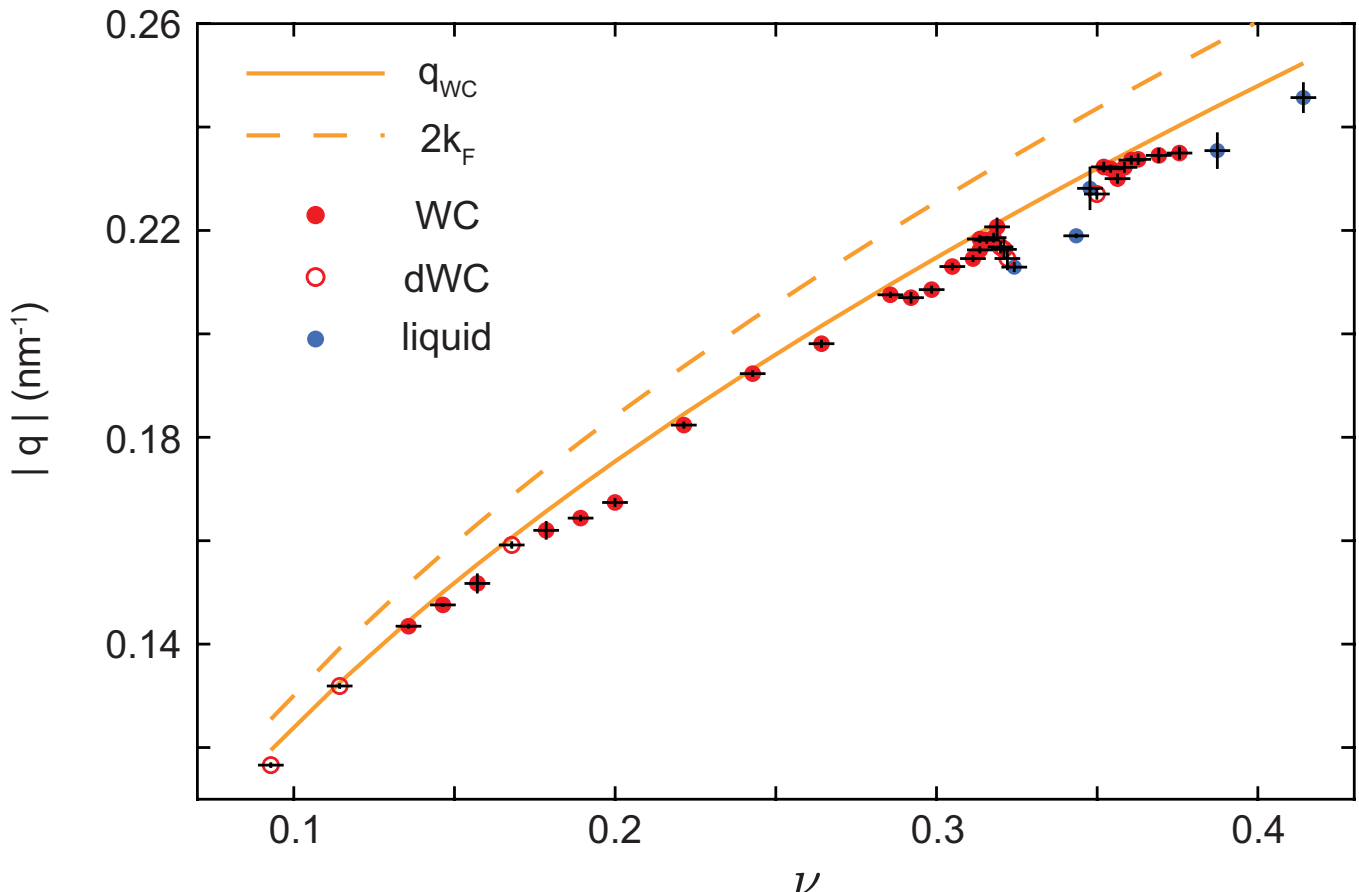


Extended Data Fig. 4 | Full data set (III) of electronic ground state imaging at $B=13.95$ T. The data are presented in the sequence in rows of δI_{dc} , $S(q)$, and autocorrelation of δI_{dc} . The filling factor ν of each set is noted on the top. The scale bars for δI_{dc} , $S(q)$, autocorrelation of δI_{dc} are 100 nm, 0.2 nm⁻¹, 100 nm, respectively.



Extended Data Fig. 5 | Phase diagram and the extracted $|\mathbf{q}|$ near the $\nu = 1/3$ FQH state at $B = 13.95 \text{ T}$. The solid line is the expected magnitude $|\mathbf{q}_{WC}|$ of the Bragg peaks of the WC. The grey mask represents where the FQHs $\nu = 1/3$ sets in. The data are presented in solid triangles (WC), hollow triangles (distorted WC),

and hollow circles (liquid). As approaching the $\nu = 1/3$ FQH state, the extracted $|\mathbf{q}|$ starts deviating away from the expected $|\mathbf{q}_{WC}|$, but still the values are very close to one another. And on both sides of the FQHs there are liquid states, signifying a solid to liquid/liquid to solid transition near $\nu = 1/3$.



Extended Data Fig. 6 | Filling factor ν dependence of the extracted $|q|$ at $B=13.95\text{ T}$. The solid line is the expected magnitude $|q_{WC}|$ of the Bragg peaks of the WC. The dashed line is the expected magnitude $|q_{FL}|$ for Fermi liquid or composite Fermi liquid, if we assume the interference pattern originates from the scattering between two opposite points $\pm k_F$ on the Fermi surface at zero magnetic field. The data are presented in filled red circle (WC), hollow red

circles (distorted WC), and filled blue circles (liquid). Most points are below $|q_{WC}|$. Interestingly, deviations of $|q_{WC}|$ are towards the direction away from $|q_{FL}|=2|k_F|=2\sqrt{4\pi n}$. The error bars in vertical direction represent the fitting error of determining $|q|$, and horizontal error bars denote the uncertainty of the filling factor ν determination (see Method).